Aggregate

WILEY

Aggregate Open Access

RESEARCH ARTICLE OPEN ACCESS

Achieving 20.1% Efficiency in Organic Solar Cells Through Interconnected Fibrillar Networks via Local Molecular Stacking

Junying Wu[1] | Wanqing You[1] | Xuanang Luo[1] | Xiaojing Wang[1] | Zhiyuan Yang[1] | Junhao Zeng[1] | Jingchuan Chen[1] | Cheng Wang[2] | Lei Ying[1] | Wenkai Zhong[1] | Zhicai He[1] | Yong Cao[1]

[1]Institute of Polymer Optoelectronic Materials and Devices, State Key Laboratory of Luminescent Materials and Devices, South China University of Technology, Guangzhou, Guangdong, China | [2]Advanced Light Source, Lawrence Berkeley National Laboratory, Berkeley, California, USA

Correspondence: Wenkai Zhong (wkzhong@scut.edu.cn) | Zhicai He (zhicaihe@scut.edu.cn)

Received: 30 November 2025 | **Revised:** 17 January 2026 | **Accepted:** 11 February 2026

Keywords: amorphous | molecular stacking | morphology | organic solar cells | post-treatments

ABSTRACT

The performance of organic solar cells (OSCs) is governed by how molecular packing evolves into interconnected networks that facilitate exciton dissociation and charge transport. Using an all-small-molecule blend DR3TSBDT:Y6 as a model system, we study how local molecular stacking evolves into performance-relevant morphology during solvent vapor annealing (SVA) and subsequent thermal annealing (TA). SVA promotes end-to-end stacking of amorphous acceptors to form interconnected fibrils, while TA compacts inter-fibril spacing without disrupting favorable local order. Such molecular-to-morphological refinements broaden light absorption, enhance charge transport, and markedly improve device efficiency. Extending this approach to additional blend systems (D18:Y6, D18:L8-BO, and DR3TSBDT:L8-BO) yields similar structural evolution and performance gains, with the D18:L8-BO system achieving up to 20.10% PCE. Our study establishes control over local stacking in amorphous acceptors into fibrillar networks as a general and effective route to realize high-performance OSCs.

1 | Introduction

Organic solar cells (OSCs) have achieved remarkable progress in recent years, with certified power conversion efficiencies (PCEs) for single-junction devices surpassing 20% [1–4]. This advance has been driven by the development of high-performance the Y-series non-fullerene acceptors (NFAs) and by improved control over active-layer morphology [5–9]. Within this context, fibrillar, high-aspect-ratio domains are widely identified as a favorable morphological motif, as they promote exciton dissociation, directional charge transport, and efficient collection [10–15]. Guided by insights from single-crystal study, many research efforts have focused on promoting favorable end-group or π–π stacking motifs by molecular design strategies, including side-chain tuning, backbone modification, and ternary blends [16–19]. In practice, tailored backbone rigidity and side-chain structures in donors, together with end-group and conjugated core design in NFAs, allow precise control of molecular packing and phase-separated morphology [20–23]. Introducing a third component to adjust donor-acceptor (D/A) interfacial compatibility can further refine molecular ordering and enhance device performance [24, 25].

Despite these advances in morphology control, a significant and underappreciated limitation remains. The molecular packing of NFAs in solution-processed active layers rarely reaches single-crystals-like order, because rapid solvent evaporation kinetically traps molecules into metastable configurations with substantial packing dislocations and defects [26, 27]. Although processing additives can modulate film-formation kinetics and generate fibrillar morphologies that enhance device efficiency, a large

fraction of amorphous states persists and continues to limit device performance [28–30].

Post-treatments such as solvent vapor annealing (SVA) and thermal annealing (TA) have therefore been used to tune such metastable molecular packing [31–34]. TA promotes the face-on molecular orientation and π–π stacking of Y6 [26, 35], yet most studies on TA have focused mainly on optimizing the crystalline phase, overlooking its role in fine-tuning molecular packing in amorphous regions. SVA provides a kinetic pathway for molecular rearrangement through the swelling effect of solvent molecules, which adjust phase separation and packing motif [33, 36]. Prior SVA studies on Y6-based systems, typically focus on the strengthening of crystalline phases, while the role of amorphous molecular packing in contributing to device performance has remained largely unexplored. Therefore, advancing beyond crystal-centric design rules, improving the amorphous local molecular packing that can evolve into performance-relevant fibrillar networks represents a crucial new direction to further unlock the efficiency potential of OSCs.

Here, using an all-small-molecule blend DR3TSBDT:Y6 as a model system, we elucidate how post-deposition treatments, SVA alone or SVA sequentially followed by TA, can unlock the latent performance potential of OSCs. These treatments induce subtle yet crucial rearrangements of amorphous stacking of Y6 into end-to-end contacts that propagates into a highly interconnected fibrillar network. Building on these insights, we further applied this strategy to the high-performing D18:Y6 and D18:L8-BO systems, achieving PCEs exceeding 19% and 20%, respectively. Our findings highlight the critical role of manipulating amorphous molecular packing in establishing functional mesoscale morphology for advancing OSC efficiency beyond crystallinity-driven design rules.

2 | Results and Discussion

2.1 | Photovoltaic Performance and Physical Analysis

Figure 1a presents the chemical structures of the donor DR3TSBDT and acceptor Y6. DR3TSBDT:Y6 is selected as a model all-small-molecule system due to its simple chemical structure and well-defined crystallization behavior, which eliminates polymer chain effects and allows clear investigation of intrinsic Y6 packing and fibril formation. As shown in Figure 1b, the blend thin films were prepared by spin-coating a chloroform solution of DR3TSBDT:Y6 (1:0.8, w/w), followed by post-deposition treatments. Carbon disulfide (CS_2) was selected for SVA owing to its low boiling point (46°C) and moderate solvation strength, which enable controlled molecular reorganization without disrupting the phase-separated morphology [37–39]. Based on systematic optimization of the SVA solvent, TA temperature, and processing time (Figure S1 and Tables S1–S3), the optimal treatments include SVA with CS_2 for 50 s and then TA at 80°C for 5 min. For simplicity, we refer to the single SVA treatment as "SVA" and the combined treatment as "SVA+TA." Normalized UV-vis-NIR absorption spectra reveal that SVA induces a pronounced redshift in the absorption of Y6, while SVA+TA slightly blue-shifts the spectral features relative to the SVA-treated film and still exhibits a redshift compared to the as-cast film (Figure 1c). Vibronic analysis of the absorption spectra reveals that SVA significantly increases the 0-0/0-1 intensity ratio of Y6 from 0.48 (as-cast) to 1.00 (Tables S4 and S5), indicating a transition toward *J*-type stacking. These spectral shifts indicate enhanced electronic coupling and effective π-conjugation, associated with improved molecular packing.

The current density–voltage (*J*–*V*) curves and corresponding device metrics are summarized in Figure 1d and Table 1. The as-cast device delivered a poor PCE of 0.44%, with an open-circuit voltage (V_{OC}) of 0.94 V, a short-circuit current density (J_{SC}) of 2.14 mA cm^{-2}, and a fill factor (FF) of 21.57%. In contrast, the SVA-treated device exhibited a dramatically improved PCE of 11.7%, with a tenfold increase in J_{SC} (23.34 mA cm^{-2}) and over twofold increase in FF (57.11%). The combined SVA+TA treatment further enhanced the PCE to 12.32%. The increase in J_{SC} aligns well with the enhanced external quantum efficiency (EQE) across the absorption range (Figure 1e). Meanwhile, V_{OC} gradually decreased from 0.94 V (as-cast) to 0.88 V (SVA) and 0.86 V (SVA+TA). This reduction is attributed to the red-shifted onset of absorption as well as EQE spectra, rather than an increase in energetic losses, as all devices exhibit similar energy loss (E_{loss}) values of ~0.55 eV (Figures 1f,g, S2, and S3 and Table S6) [40, 41].

To study recombination behavior, light-intensity (P_{light}) dependence of V_{OC} was analyzed via extracting the *n* factors with $V_{OC} \propto \frac{nkT}{q} \ln(P_{light})$ [42], where *k* represents the Boltzmann constant, *T* is the absolute temperature, *q* is the elementary charge, and P_{light} refers to the incident light intensity. The extracted *n* factors were 1.16 and 1.05 for the SVA and SVA+TA devices, respectively, indicating suppressed trap-assisted recombination (Figure 1h and Table S7) [43]. These findings are consistent with the reduced energetic disorder observed in the trap density of states (tDoS), as shown in Figure 1i. Exciton dissociation and carrier collection efficiencies were evaluated using the photocurrent density (J_{ph}) versus effective voltage (V_{eff}) characteristics (Figure 1j) [44, 45]. The as-cast device exhibited slow carrier release at high bias, indicative of severe trap-induced recombination and charge loss. In contrast, the SVA and SVA+TA devices showed saturation of J_{ph} in the high-bias region, confirming near-complete exciton dissociation and efficient charge extraction. The ratio of J_{ph} to J_{sat} under short-circuit conditions increased to 89% for the SVA+TA device, further supporting reduced trap density and enhanced collection efficiency. Charge carrier transport was evaluated via the photo-CELIV method (Figure 1k) [46]. The SVA and SVA+TA devices both exhibited carrier mobilities of ~2×10^{-4} cm^2 V^{-1} s^{-1}, ~40 times higher than the as-cast device (~5×10^{-6} cm^2 V^{-1} s^{-1}). Taken together, the improvements in exciton dissociation, charge transport, and carrier collection efficiency can be attributed to reduced energetic disorder and suppressed trap-assisted recombination enabled by the post-treatments.

To further justify the focus on SVA and SVA+TA treatments, we compared the effects of TA-only and TA+SVA on device performance (Figure S4). As summarized in Table S8, TA along significantly improves the PCE of DR3TSBDT:Y6 devices to 11.39%. However, although TA+SVA leads to further performance enhancement, its PCE remained lower than that obtained by SVA+TA. This comparison highlights that TA alone cannot

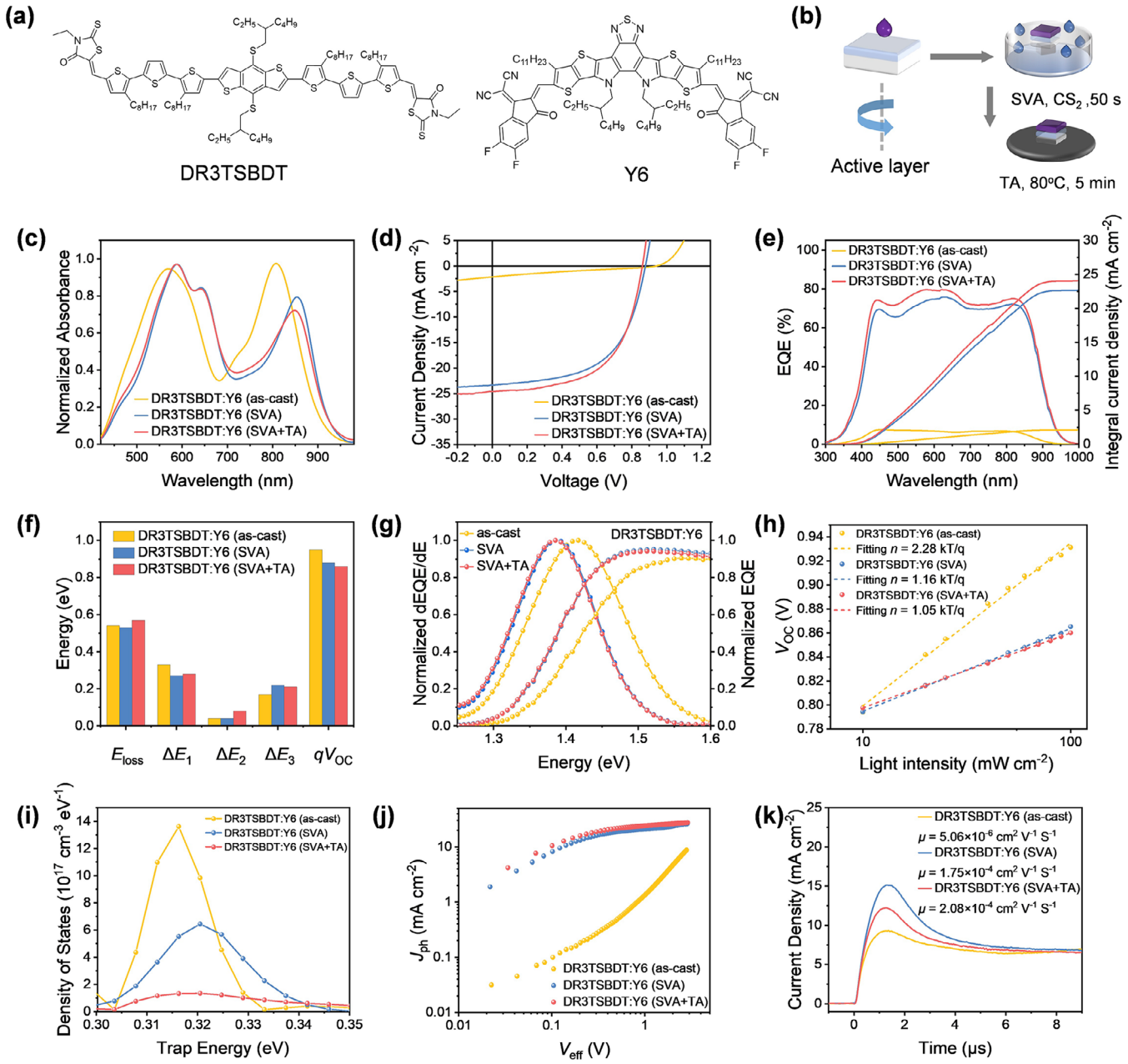

FIGURE 1 | (a) Chemical structures of DR3TSBDT and Y6. (b) Schematic illustration of post-treatment protocols: SVA followed by TA applied to DR3TSBDT:Y6 blend films. (c) Normalized UV-vis-NIR absorption spectra of DR3TSBDT:Y6 films under different post-treatments. (d) *J*–*V* curves, (e) EQE spectra, (f) E_{loss} analysis, (g) first derivative of EQE spectra, (h) light-intensity dependence of V_{OC}, (i) tDoS, (j) J_{ph}-V_{eff} characteristics, and (k) photo-CELIV curves of DR3TSBDT:Y6 OSC devices with different post-treatments.

TABLE 1 | Photovoltaic parameters of DR3TSBDT:Y6 based OSC devices.

Device	V_{OC}[a] [V]	J_{SC}[a] [mA cm^{-2}]	$J_{SC,\,EQE}$[b] [mA cm^{-2}]	FF[a] [%]	PCE[a] [%]
as-cast	0.94 (0.93 ± 0.012)	2.14 (2.04 ± 0.083)	2.09	21.57 (21.45 ± 0.32)	0.44 (0.41 ± 0.018)
SVA	0.88 (0.88 ± 0.008)	23.34 (23.22 ± 0.33)	22.64	57.11 (56.79 ± 0.57)	11.70 (11.54 ± 0.20)
SVA+TA	0.86 (0.86 ± 0.005)	24.59 (24.26 ± 0.29)	24.03	58.24 (58.18 ± 0.30)	12.32 (12.25 ± 0.08)

[a]Measured by *J*–*V* curves with device of ITO/PEDOT: PSS/active layer/PDINO/Ag.
[b]Integrated J_{SC} from EQE curves.

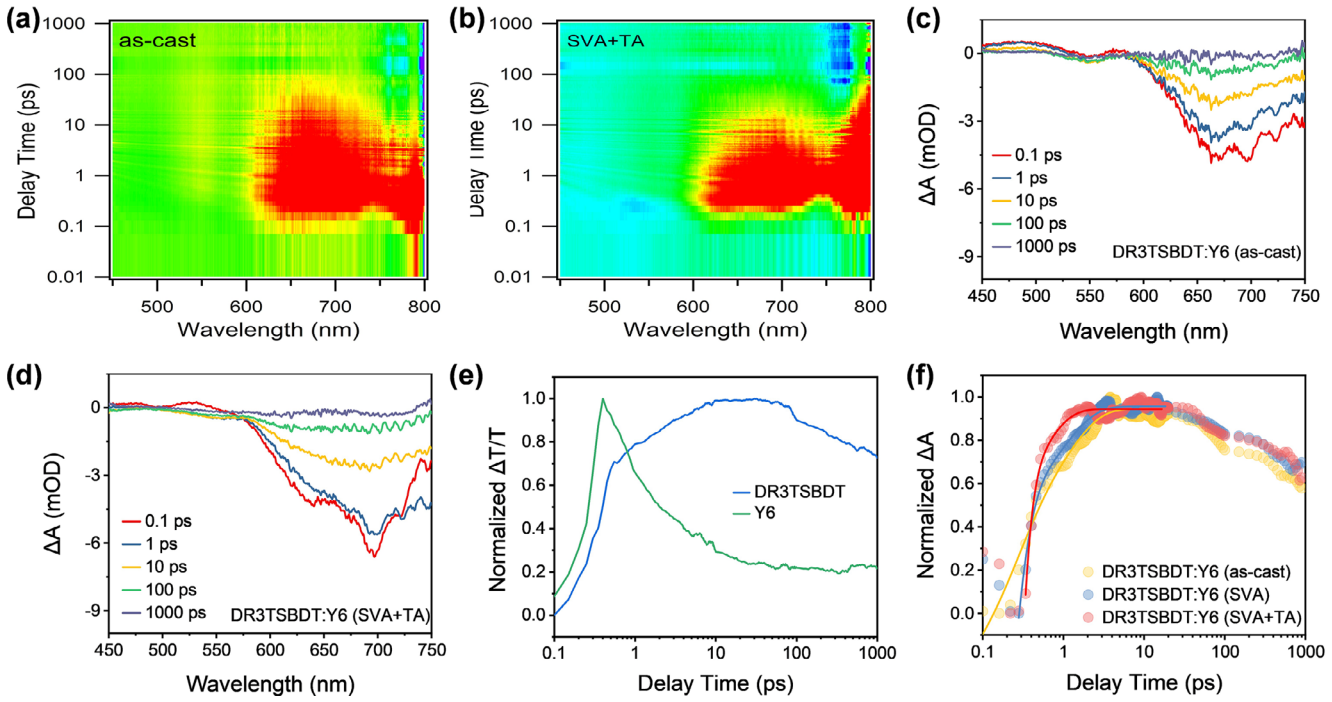

FIGURE 2 | Contour maps of fs-TA spectra for DR3TSBDT:Y6 blend films: (a) as-cast and (b) after SVA+TA treatment under 800 nm excitation. Representative fs-TA spectra at selected delay times for (c) as-cast and (d) SVA+TA-treated films. (e) Hole transfer dynamics in the SVA+TA-treated blends revealed by the GSB kinetics of DR3TSBDT at 500 nm and Y6 at 700 nm. (f) GSB kinetics at 550 nm for three blend films with corresponding biexponential fits.

induce favorable local molecular stacking rearrangement, whereas SVA initializes such stacking and enables TA to effectively consolidate the morphology for maximizing device performance.

2.2 | Exciton Diffusion and Dissociation

To elucidate the role of post-treatments on exciton dynamics, femtosecond transient absorption (fs-TA) spectroscopy was used to probe exciton diffusion and dissociation processes [47, 48]. Owing to the non-negligible absorption of Y6 at ~550 nm in the steady-state spectra (Figure S5), excitation at this wavelength would simultaneously populate both donor and acceptor states. Therefore, an 800 nm pump was selected to selectively excite Y6 and initiate the hole-transfer process in the blend films. Under 800 nm excitation, fs-TA measurements of neat films show that neat Y6 exhibits a distinct ground-state bleach (GSB) signal in the 650–750 nm with no response at 550 nm, whereas neat DR3TSBDT displays no GSB in the 650–750 nm but has intrinsic absorption characteristics at 550 nm (Figure S6). These spectral fingerprints enable assignment of the 650–750 nm GSB to Y6 and the ~550 nm GSB to DR3TSBDT in the blend films [49–51].

We then excited Y6 at 800 nm to initiate the hole-transfer process from Y6 to DR3TSBDT. Figures 2a,b and S7a display the 2D contour images of fs-TA spectra for the as-cast, SVA+TA-treated and SVA-treated films, while Figures 2c,d and S7b present representative spectra at selected time delays. In all cases, a GSB signal corresponding to Y6 appears between 650–750 nm immediately after excitation. Subsequently, a bleach feature emerges ~550 nm, matching the absorption of DR3TSBDT. The decay of the Y6 bleach coincides with the rise of the DR3TSBDT bleach (Figure 2e), confirming ultrafast hole transfer from Y6 to DR3TSBDT across the D/A interface.

Exciton dissociation dynamics were quantified by fitting the decay kinetics at 550 nm with a biexponential model (Figure 2f). The extracted time constants τ_1 and τ_2 correspond to exciton dissociation at the D/A interface and exciton diffusion toward the interface, respectively [52, 53]. In the as-cast film, τ_1 = 0.213 ps and τ_2 = 1.053 ps. After SVA treatment, both values decrease to 0.103 ps and 0.904 ps, and further reduce to 0.072 ps and 0.409 ps following SVA+TA processing. Notably, the subsequent TA treatment after SVA leads to a more pronounced reduction in the exciton diffusion time τ_2, reduced by 61% relative to the as-cast film and by 54.9% relative to the SVA-treated film (Table S9). This indicates that TA treatment further consolidates the molecular stacking and energetic landscape established by SVA, thereby providing more efficient exciton diffusion and dissociation pathways.

Photoluminescence (PL) spectroscopy (excitation at 550 nm, Figure S8) was used to probe interfacial exciton quenching and charge transfer process. In the blend films, the donor PL at 704 nm is almost completely quenched, while a redshifted emission appears at 814 nm, consistent with charge-transfer excitons. The sustained strong PL quenching for the SVA and SVA+TA blends is in agreement with the accelerated exciton dissociation observed by fs-TA and the improved device performance. Therefore, the modest improvement in exciton kinetics (Table S9), together with enhanced charge mobility and reduced defect states, leads to the substantial J_{SC} and FF enhancements in the post-treated devices. These findings suggest that SVA and SVA+TA improve

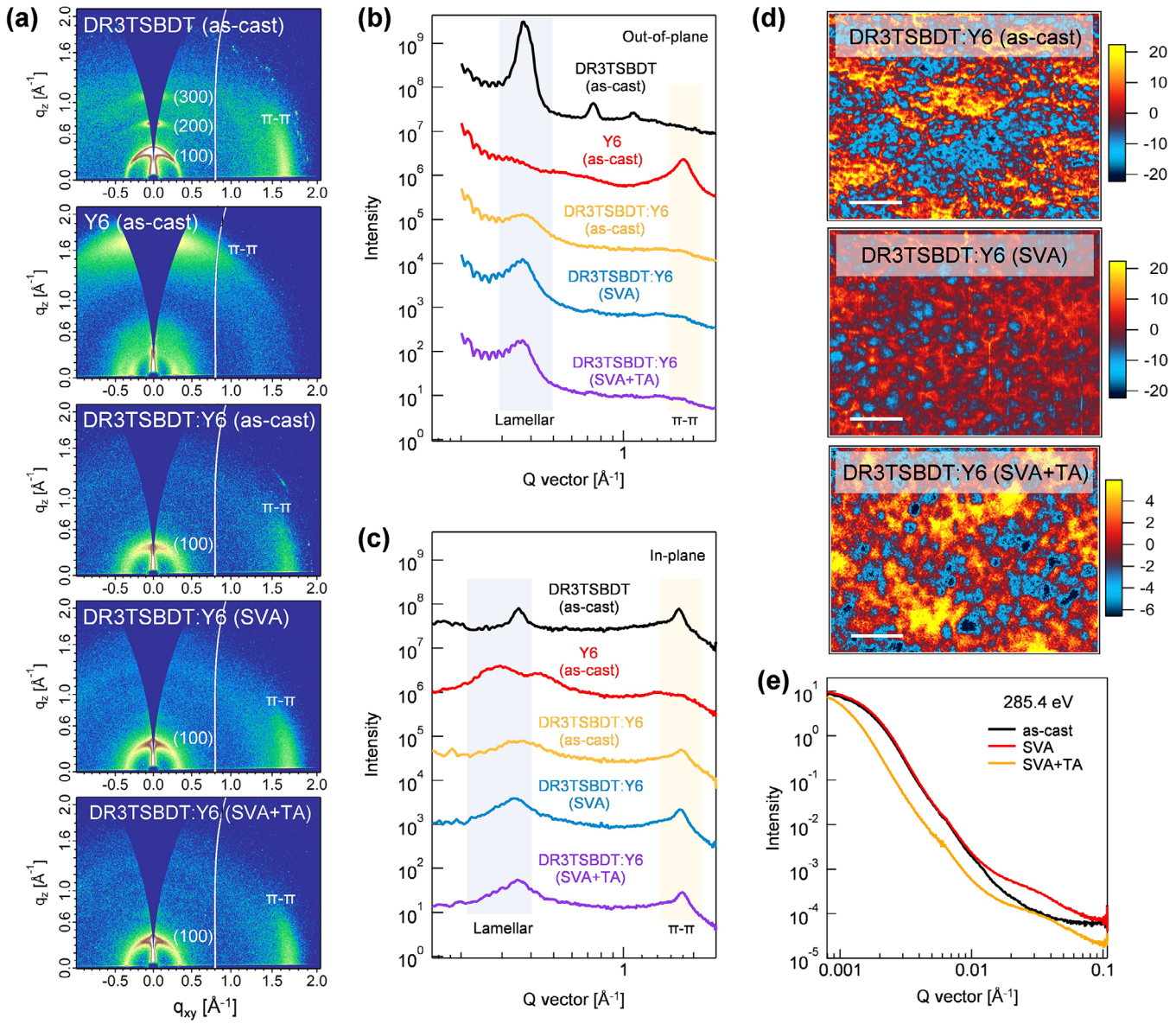

FIGURE 3 | (a) GIWAXS patterns of DR3TSBDT, Y6, and DR3TSBDT:Y6 blend films under different post-treatments. GIWAXS *I*–*q* curves in the (b) OOP and (c) IP directions. (d) AFM-IR images of DR3TSBDT:Y6 blend films. The scale bar represents 200 nm and the color bar corresponds to the IR amplitude in arbitrary units (a.u.). (e) RSoXS *I*–*q* curves of DR3TSBDT:Y6 blend films.

the multiscale film structure, from local molecular stacking to phase-separated morphology, facilitating more efficient charge carrier generation.

2.3 | Molecular-to-Morphological Analysis

Grazing-incidence wide-angle X-ray scattering (GIWAXS) reveals crystalline packing in neat and blend films (Figure 3a–c). In neat films, DR3TSBDT exhibits an edge-on orientation, as indicated by a strong π–π stacking reflection at 1.75 Å^{-1} in the in-plane (IP) direction and high-order lamellar reflections in the out-of-plane (OOP) direction. In contrast, Y6 adopts a face-on orientation, with a π–π stacking peak at 1.81 Å^{-1} in the OOP direction and a lamellar (0.30 Å^{-1}) reflection in the IP direction. In the blend films, the scattering patterns are primarily associated with DR3TSBDT, which preserves characteristic edge-on orientation with comparable peak positions for both π–π stacking and lamellar reflections after SVA and SVA+TA. SVA induces a modest enhancement in the ordering of DR3TSBDT, as evidenced by the increased reflection intensity, whereas introducing TA after SVA does not lead to further crystallinity enhancement (Table S10). Nevertheless, the absence of high-order lamellar (200) and (300) reflections in the blend films indicates that DR3TSBDT crystallites are weakened or partially disrupted by blending, rather than being altered by post-treatments. Meanwhile, UV-vis-NIR absorption spectra of the blend films show a slight redshift accompanied by the emergence of a shoulder feature for DR3TSBDT (~600 nm) after post-treatment, suggesting improved chain packing and an increased effective conjugation length associated with enhanced short-range aggregation. However, such spectral evolution does not translate into increased crystallinity. These results indicate that the blend films consist of weak DR3TSBDT crystallites embedded in a largely amorphous DR3TSBDT:Y6 matrix,

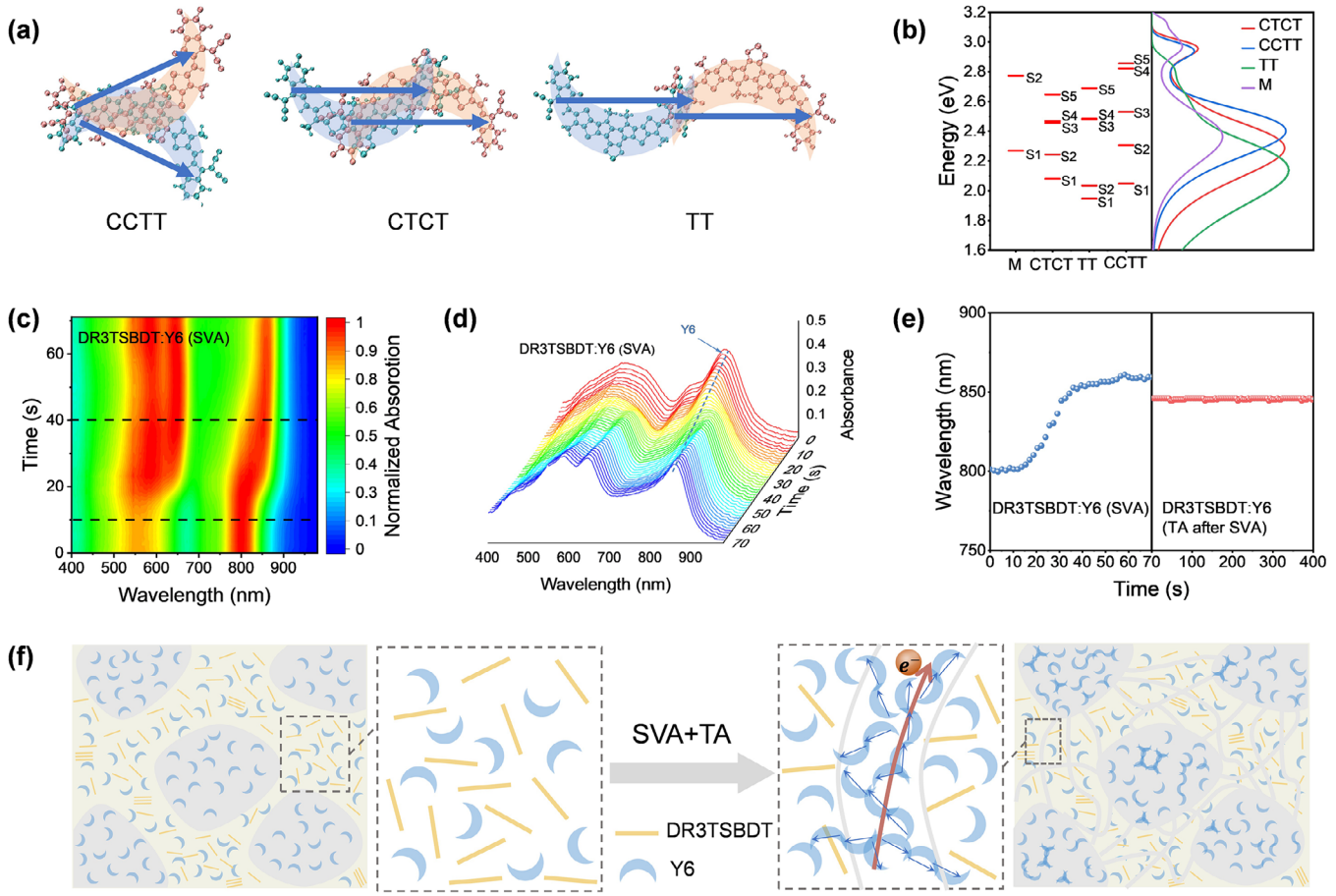

FIGURE 4 | (a) Schematic of three representative Y6 dimer stacking configurations: CCTT, CTCT, and TT. (b) TD-DFT calculated vertical excited-state levels and corresponding absorption spectra of different stacking configurations, where "M" represents single molecule. (c) Contour plots and (d) line profiles of in situ UV-vis-NIR spectra of DR3TSBDT:Y6 blend films during CS_2-SVA treatment. (e) Evolution of Y6 absorption peak position as a function of SVA and TA time. (f) Schematic illustration of interconnected fibrils formed via local molecular stacking during SVA+TA treatment.

where the post-treatment-induced morphological optimization predominantly arises from local molecular rearrangement.

The morphology of DR3TSBDT:Y6 blend films under as-cast, SVA, and SVA+TA conditions was imaged by transmission electron microscopy (TEM) and atomic force microscopy-infrared (AFM-IR). In all cases, TEM images show pronounced light/dark contrast arising from the electron density difference between the donor and acceptor phases, evidencing clear phase separation (Figure S9a–c). To obtain chemical-specific insight, AFM-IR mapping of the 1295 cm^{-1} vibrational mode was used to visualize Y6 domains (Figures 3d, S10 and S11). In the as-cast film, Y6 forms large aggregates, whereas SVA treatment induces interconnected fibrillar structures bridging adjacent Y6 domains. Here, fibrillar structures refer to elongated, interconnected domains arising from directional molecular stacking [54, 55]. While DR3TSBDT shows lamellar reflection enhancement and minor absorption red-shifts, its contribution to these fibrillar features remains uncertain. Subsequent SVA+TA processing further enlarges the Y6 domains while preserving these fibrillar connections. Resonant soft X-ray scattering (RSoXS) at 285.4 eV supports this trend (Figures 3e and S12–S14). The averaged I–q curves show a strong low-q scattering feature for all blends, corresponding to large-scale phase separation (~445 nm for as-cast and SVA; ~660 nm for SVA+TA). Crucially, SVA introduces an additional feature at 0.033 $Å^{-1}$ (~19 nm), attributed to the inter-fibril spacing in-between Y6 aggregates, which TA reduces to ~15 nm [56], densifying the fibrillar network. Collectively, these results demonstrate that post-treatments promote preserve and densify interconnected fibrillar networks that facilitate exciton dissociation and charge transport, thereby enhancing J_{SC} and FF in the devices.

Given the largely amorphous character of Y6 in the blends, the emergence of fibrils after post-treatment is most plausibly driven by reorganization of amorphous Y6 across the phase-separation scale, along with a pronounced red shift in the absorption (~50 nm). To examine the molecular origin of this spectral evolution, we performed time-dependent density functional theory (TD-DFT) calculations of vertical excitation energies for Y6 dimers in three representative stacking motifs, including CCTT, CTCT, and TT, which have been previously identified by molecular dynamics and single-crystal fragments (Figure 4a) [57–59]. These motifs differ in the relative orientation of the molecular core (C) and terminal (T) groups and thus in the slip angle between transition dipoles. Our calculations show a systematic red shift of the lowest allowed transition in the sequence CCTT → CTCT → TT (Figure 4b), with the

TT dimer exhibiting the smallest slip angle. Within the Kasha framework, variations in transition-dipole geometry redistribute oscillator strength between excitonic states: parallel dipoles (*H*-type) favor higher-energy allowed transitions (blue shift), whereas end-to-end dipoles (*J*-type) render the lower-energy transition allowed (red shift) (Figure S15) [60–62]. The computed trends in excitation energies and oscillator strengths therefore align with the experimentally observed red shift, suggesting that SVA promotes reorganization of Y6 toward *J*-type stacking that enhances intermolecular conjugation in the thin film. Additional TD-DFT calculations were conducted on DR3TSBDT dimers with H-type, TT, and TDTD configurations (Figure S16). While dimerization enhances absorption intensity and induces a gradual red shift toward more *J*-like motifs, the magnitude of the shift remains modest, matching the slight red shift observed experimentally. These results reveal a clear asymmetry in donor-acceptor responses: while both components undergo local packing evolution, pronounced morphological and electronic reorganization occurs predominantly in the amorphous acceptor phase.

In-situ UV-vis-NIR absorption spectroscopy during SVA reveals a gradual red shift of the Y6 absorption peak following a sigmoidal time dependence, characterized by an induction period, a rapid transition, and subsequent saturation (Figures 4c–e and S17). This kinetic profile indicates that SVA first nucleates *J*-type packing, which then propagates cooperatively at the mesoscale. The magnitude of the spectral shift, together with AFM-IR and RSoXS evidence for increasing fibrillar connectivity and the TD-DFT results, points to the reorganization of amorphous Y6 toward a locally *J*-dominated packing. Among possible *J*-type configurations, TT stacking is the most plausible motif, owing to minimal alkyl-chain steric hindrance, as supported by single-crystal analyses and our DFT calculations (Figure S18). TT stacking also exhibits a relatively high electronic coupling (0.024 eV, compared with 0.015 eV for CTCT and 0.029 eV for CCTT; Table S11), facilitating efficient intermolecular charge transport. Notably, this TT stacking represents a local, short-range packing motif occurring within largely amorphous Y6 domains, rather than a long-range crystalline order. The extended π–π overlap of TT dimers through multiple end-to-end contacts forms fibrillar Y6 networks that bridge larger-scale domains (Figure S19). Subsequent TA induces a slight blue shift without disrupting such end-to-end packing, instead consolidating the fibrillar network by reducing inter-spacing, reflecting geometric or electrostatic adjustment rather than structural breakdown. These molecular and morphological evolutions extend light-harvesting via red-shifted end-to-end stacking and improve charge-carrier mobility by strengthened π–π connectivity, rationalizing the enhanced PCE of post-treated devices. A schematic illustration of the interconnected fibrillar networks formed during SVA+TA treatment is shown in Figure 4f.

2.4 | Generality of Local Molecular Stacking Control Guideline

To verify the generality of the local molecular stacking optimization for efficient OSCs, we extended this guideline to two additional NFA-based systems: D18:Y6 and D18:L8-BO (Figure 5a). The *J*–*V* curves and performance parameters of the OSC devices are summarized in Figures 5b,c and S20 and Tables 2 and S12. For D18:Y6 blend, the PCE increases from 17.83% (as-cast) to 18.27% (SVA) and 19.10% (SVA+TA, V_{OC} = 0.845 V, J_{SC} = 28.10 mA cm^{-2}, FF = 80.44%). Similarly, the D18:L8-BO devices improve from 18.04% to 19.45% (SVA) and 20.10% (SVA+TA, V_{OC} = 0.910 V, J_{SC} = 27.35 mA cm^{-2}, FF = 80.75%). Although V_{OC} slightly decreases, the substantial gains in J_{SC} and FF drive the overall PCE improvements. The EQE spectra show enhanced photocurrent response across the full wavelength range (Figure S21), indicating more efficient charge generation and collection. The 20.10% efficiency achieved for D18:L8-BO devices represent a new benchmark for this system without any processing additive (Figure 5d and Table S13). The reduction in V_{OC} for D18-based devices after SVA and SVA+TA treatments is significantly smaller than that observed in the DR3TSBDT:Y6 system. This is primarily because DR3TSBDT:Y6 is an all-small-molecule blend, where Y6 readily diffuses and reorganizes under SVA to form strong *J*-type packing, leading to pronounced absorption redshift and a substantial decrease in V_{OC}. In contrast, in D18-based polymer systems, the motion of acceptor molecules is constrained by the polymer chains, limiting molecular reorganization and resulting in weaker *J*-type packing and thus marginal V_{OC} loss.

For both systems, UV-vis-NIR absorption spectra reveal that SVA induces a significant red shift of the NFA absorption, followed by a slight blue shift after TA (Figure 5e,f), mirroring the behavior observed for the DR3TSBDT:Y6 blend. Taking the D18:L8-BO blend as an example, although the absorption of D18 changes slightly, a distinct red-shift occurs in L8-BO. In situ spectroscopy shows that the red shift of the L8-BO absorption during SVA has a sigmoidal time dependence (Figures 5g and S22), consistent with the end-to-end packing nucleation and cooperative propagation observed in the DR3TSBDT:Y6 system. AFM-IR maps of the L8-BO domains reveal analogous morphological transitions (Figure S23). As shown in Figure 5i–k, after SVA, interconnected fibrillar structures bridging adjacent L8-BO domains appear, while SVA+TA further enhances such domain interconnection. RSoXS supports these trends (Figures 5h and S24–S26), with an interference feature at 0.02 Å^{-1}, corresponding to an inter-fibril distance of ~31 nm. These results demonstrate that promoting end-to-end stacking of amorphous acceptors, which propagates into interconnected fibrillar networks, provides a general and practical guideline for advancing diverse OSC blend systems toward their performance limits. Thermal stability tests further show that after 216 h of aging at 80°C, the SVA+TA-treated DR3TSBDT:Y6 and D18:L8-BO devices consistently exhibit enhanced PCE retention, compared to their as-cast and SVA-only counterparts (Figure S27; Tables S14–S17). Such improved stability can be attributed to the amorphous-dominated, interconnected fibrillar network, where exciton dissociation and charge transport are less sensitive to local packing fluctuations under thermal stress (Figures S27, S28).

We further fabricated DR3TSBDT:L8-BO devices to validate the generality of this strategy (Figure S29 and Table S18). Upon SVA+TA treatment, the PCE enhances from 0.39% (as-cast) to 13.93%, with J_{SC} and FF improvements, further supporting the general applicability of the local molecular stacking regulation in OSCs. Based on the blend systems studied, the suitability

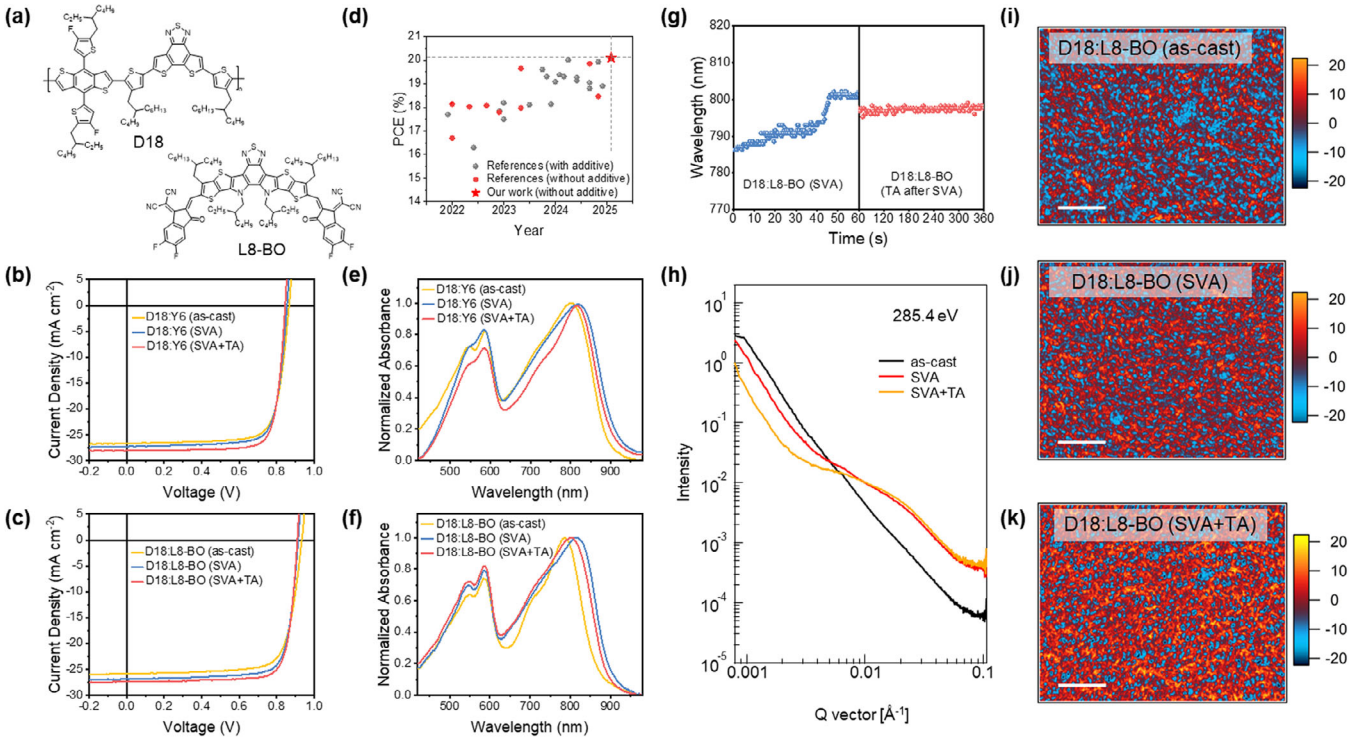

FIGURE 5 | (a) Chemical structures of D18 and L8-BO. *J–V* curves of OSCs based on (b) D18:Y6 and (c) D18:L8-BO blends with different post-treatments. (d) Reported PCE values of D18:L8-BO based OSCs. Normalized UV-vis-NIR absorption spectra of (e) D18:Y6 and (f) D18:L8-BO blend films with different post-treatments. (g) Evolution of L8-BO absorption peak position as a function of SVA and TA time. (h) RSoXS *I–q* curves at 285.4 eV of D18:L8-BO blend films. AFM-IR images of D18:L8-BO blend films with different post-treatments: (i) as-cast, (j) SVA, and (k) SVA+TA. The images were measured 1344 cm^{-1} vibrational mode to highlight the L8-BO domains. The scale bar represents 200 nm and the color bar corresponds to the IR amplitude in arbitrary units (a.u.).

TABLE 2 | Photovoltaic parameters of D18:Y6 and D18:L8-BO based OSC devices.

Blend	Device	V_{OC}[a] [V]	J_{SC}[a] [mA cm^{-2}]	$J_{SC,EQE}$[b] [mA cm^{-2}]	FF[a] [%]	PCE[a] [%]
D18:Y6	as-cast	0.866 0.861 ± 0.008	26.67 26.62 ± 0.141	26.09	77.25 77.01 ± 0.171	17.83 17.72 ± 0.117
	SVA	0.854 0.850 ± 0.005	27.32 27.15 ± 0.174	26.82	78.27 78.11 ± 0.289	18.27 18.2 ± 0.14
	SVA+TA	0.845 0.840 ± 0.005	28.10 27.89 ± 0.105	27.46	80.44 80.28 ± 0.119	19.10 19.07 ± 0.091
D18: L8-BO	as-cast	0.933 0.929 ± 0.004	25.55 25.43 ± 0.120	25.05	75.69 75.39 ± 0.375	18.04 17.95 ± 0.095
	SVA	0.914 0.911 ± 0.003	26.92 26.87 ± 0.066	26.26	79.03 78.84±0.215	19.45 19.36 ± 0.090
	SVA+TA	0.910 0.906 ± 0.003	27.35 27.29 ± 0.072	26.68	80.75 80.59 ± 0.168	20.10 19.99 ± 0.110

[a]Measured by *J–V* curves with device structure of ITO/PEDOT: PSS/2PACz/active layer/PDINN/Ag.
[b]Integrated J_{SC} from EQE curves.

of D:A combinations for this strategy can be assessed by three guidelines: (1) the acceptor allows end-to-end rearrangement and locally *J*-type stacking under post-treatment; (2) the D:A pair maintains moderate phase separation during SVA, enabling local rearrangement without morphological collapse; (3) a sigmoidal red-shift evolution in in-situ UV-vis-NIR absorption during SVA serves as a rapid indicator of fibrillar network formation.

3 | Conclusion

We demonstrate that controlled promotion of end-to-end packing in amorphous NFAs drives the formation of performance-relevant fibrillar morphology in OSCs. Such molecular-to-morphological manipulation can be effectively achieved through post-treatments like SVA and SVA+TA. The interconnected fibrils formed via acceptor reorganization markedly enhance exciton

dissociation and charge transport, thereby boosting device performance. Extending this strategy to additional blends, including D18:L8-BO, yields similar structural evolution and efficiency improvements, achieving a 20.10% PCE. Our findings indicate that controlling local molecular stacking in amorphous acceptors to promote reorganization into interconnected fibrils represents a general and effective route to unlock the efficiency potential of OSCs.

4 | Experimental Section

See experimental details in the Supporting Information.

Author Contributions

Junying Wu: investigation, writing – original draft, writing – review & editing. **Wanqing You:** formal analysis. Xuanang Luo: formal analysis. **Xiaojing Wang:** investigation. **Zhiyuan Yang:** investigation. **Junhao Zeng:** investigation. **Jingchuan Chen:** investigation. **Cheng Wang:** resources. **Lei Ying:** supervision. **Wenkai Zhong:** conceptualization, writing – original draft, writing – review & editing, supervision, funding acquisition. **Zhicai He:** conceptualization, writing – original draft, writing – review & editing, supervision, funding acquisition. **Yong Cao:** project administration.

Acknowledgments

This work was financially supported by the National Key Research and Development Program of China (2023YFE0208500), the Guangdong Basic and Applied Basic Research Foundation (2025A1515011099), Fundamental Research Funds for the Central Universities (2024ZYGXZR076), and Guangzhou Basic and Applied Basic Research Project (2025A04J3912). RSoXS was performed at beamline 11.0.1.2 at the Advanced Light Source, a US DOE Office of Science User Facility under contract no. DE-AC02-05CH11231.

Conflicts of Interest

The authors declare no conflict of interest.

Data Availability Statement

The data that support the findings of this study are available from the corresponding author upon reasonable request.

References

1. J. Zhang, X. Duan, X. Li, et al., "Achieving 20% Efficiency in Binary Organic Solar Cells With Suppressed Non-Radiative Recombination via Triphenylamine Halides," *Energy & Environmental Science* 18 (2025): 5378–5388.

2. H. Chen, Y. Huang, R. Zhang, et al., "Organic Solar Cells With 20.82% Efficiency and High Tolerance of Active Layer Thickness Through Crystallization Sequence Manipulation," *Nature Materials* 24 (2025): 444–453.

3. C. Li, J. Song, H. Lai, et al., "Non-Fullerene Acceptors With High Crystallinity and Photoluminescence Quantum Yield Enable >20% Efficiency Organic Solar Cells," *Nature Materials* 24 (2025): 433–443.

4. H. Mou, Y. Yin, H. Chen, et al., "Transient Dipole Strategy Boosts Highly Oriented Self-Assembled Monolayers for Organic Solar Cells Approaching 21% Efficiency," *Journal of the American Chemical Society* 147 (2025): 21241–21251.

5. J. Wang, Y. Xie, K. Chen, H. Wu, J. M. Hodgkiss, and X. Zhan, "Physical Insights Into Non-Fullerene Organic Photovoltaics," *Nature Reviews Physics* 6 (2024): 365–381.

6. Y. Sun, L. Wang, C. Guo, et al., "π-Extended Nonfullerene Acceptor for Compressed Molecular Packing in Organic Solar Cells to Achieve Over 20% Efficiency," *Journal of the American Chemical Society* 146 (2024): 12011–12019.

7. D. Li, N. Deng, Y. Fu, et al., "Fibrillization of Non-Fullerene Acceptors Enables 19% Efficiency Pseudo-Bulk Heterojunction Organic Solar Cells," *Advanced Materials* 35 (2023): 2208211.

8. H. M. Kwon, S. V. Barma, L. Zuo, et al., "Highly Efficient Organic Solar Cells Based on S,N-Heteroacene Non-Fullerene Acceptors," *Chemistry of Materials* 30 (2018): 5429–5434.

9. M. Deng, X. Xu, Y. Duan, L. Yu, R. Li, and Q. Peng, "Y-Type Non-Fullerene Acceptors With Outer Branched Side Chains and Inner Cyclohexane Side Chains for 19.36% Efficiency Polymer Solar Cells," *Advanced Materials* 35 (2023): 2210760.

10. F. Sun, J. Wu, B. Cheng, et al., "Constructing Continuous Acceptor Fibrillar Networks and Achieving Uniform Phase Separation via Polymer-Assisted Morphology Control for 20.3% Efficiency Additive-Free Organic Solar Cells," *Energy & Environmental Science* 18 (2025): 7071–7081.

11. L. Zhu, M. Zhang, J. Xu, et al., "Single-Junction Organic Solar Cells With Over 19% Efficiency Enabled by a Refined Double-Fibril Network Morphology," *Nature Materials* 21 (2022): 656–663.

12. W. Zhong, S. Wang, and F. Liu, "Unlocking Functional Potentials: Nanofibril Networks in Organic Semiconductors," *Advanced Nanocomposites* 2 (2025): 124–147.

13. M. Zhou, C. Liao, Y. Duan, et al., "19.10% Efficiency and 80.5% Fill Factor Layer-by-Layer Organic Solar Cells Realized by 4-Bis(2-Thienyl)Pyrrole-2,5-Dione Based Polymer Additives for Inducing Vertical Segregation Morphology," *Advanced Materials* 35 (2023): 2208279.

14. F. Qi, L. O. Jones, K. Jiang, et al., "Regiospecific N -Alkyl Substitution Tunes the Molecular Packing of High-Performance Non-Fullerene Acceptors," *Materials Horizons* 9 (2022): 403–410.

15. Z. Li, J. Xie, W. Wang, et al., "Achieving 19.6% Efficiency in Organic Photovoltaics Through Guest-Polymer Assisted Morphological Fibrillization," *Energy & Environmental Science* 18 (2025): 3026–3035.

16. X. Zhang, X. Li, X. Kong, et al., "Fine-Tuning of Molecular Self-Assembly Morphology via Synergistic Ternary Copolymerization and Side Chain Optimization of Low-Cost Polymer Donors toward Efficient Organic Solar Cells," *Advanced Materials* 37 (2025): 2503325.

17. L. Xue, Q. Xie, W. Xie, et al., "Precise Side-Chain Engineering Optimizes Polymer Pre-Aggregation and Crystallinity for Efficient Organic Solar Cells with Minimized Non-Radiative Energy Loss," *Aggregate* 6 (2025): e70103.

18. L. Ye, K. Weng, J. Xu, et al., "Unraveling the Influence of Non-Fullerene Acceptor Molecular Packing on Photovoltaic Performance of Organic Solar Cells," *Nature Communications* 11 (2020): 6005.

19. Z. Chen, J. Ge, W. Song, et al., "20.2% Efficiency Organic Photovoltaics Employing a π-Extension Quinoxaline-Based Acceptor With Ordered Arrangement," *Advanced Materials* 36 (2024): 2406690.

20. J. Zhou, L. Wang, C. Liu, et al., "Tuning of the Polymeric Nanofibril Geometry via Side-Chain Interaction Toward 20.1% Efficiency of Organic Solar Cells," *Journal of the American Chemical Society* 146 (2024): 34998–35006.

21. B. Fan, W. Gao, X. Wu, et al., "Importance of Structural Hinderance in Performance–stability Equilibrium of Organic Photovoltaics," *Nature Communications* 13 (2022): 5946.

22. Y. Fu, T. H. Lee, Y.-C. Chin, et al., "Molecular Orientation-Dependent Energetic Shifts in Solution-Processed Non-Fullerene Acceptors and Their Impact on Organic Photovoltaic Performance," *Nature Communications* 14 (2023): 1870.

23. X. Liu, Z. He, H. Wang, et al., "Unraveling Cross-Scale Fluorination Mechanisms in Non-Fullerene Acceptors for High-Efficiency Organic Photovoltaics," *Advanced Functional Materials* 36 (2025): e17542.

24. N. Gasparini, A. Salleo, I. McCulloch, and D. Baran, "The Role of the Third Component in Ternary Organic Solar Cells," *Nature Reviews Materials* 4 (2019): 229–242.

25. Y. Cai, Y. Li, R. Wang, et al., "A Well-Mixed Phase Formed by Two Compatible Non-Fullerene Acceptors Enables Ternary Organic Solar Cells With Efficiency Over 18.6%," *Advanced Materials* 33 (2021): 2101733.

26. L. Zhu, M. Zhang, G. Zhou, et al., "Efficient Organic Solar Cell With 16.88% Efficiency Enabled by Refined Acceptor Crystallization and Morphology With Improved Charge Transfer and Transport Properties," *Advanced Energy Materials* 10 (2020): 1904234.

27. C. Li, J. Zhou, J. Song, et al., "Non-Fullerene Acceptors With Branched Side Chains and Improved Molecular Packing to Exceed 18% Efficiency in Organic Solar Cells," *Nature Energy* 6 (2021): 605–613.

28. J. Song, M. Zhang, T. Hao, et al., "Design Rules of the Mixing Phase and Impacts on Device Performance in High-Efficiency Organic Photovoltaics," *Research* 2022 (2022): 9817267.

29. M. Ghasemi, H. Hu, Z. Peng, et al., "Delineation of Thermodynamic and Kinetic Factors That Control Stability in Non-Fullerene Organic Solar Cells," *Joule* 3 (2019): 1328–1348.

30. K. An, W. Zhong, F. Peng, et al., "Mastering Morphology of Non-Fullerene Acceptors Towards Long-Term Stable Organic Solar Cells," *Nature Communications* 14 (2023): 2688.

31. J. Guo, B. Qiu, X. Xia, et al., "Miscibility Regulation and Thermal Annealing Induced Hierarchical Morphology Enables High-Efficiency All-Small-Molecule Organic Solar Cells Over 17%," *Advanced Energy Materials* 13 (2023): 2300481.

32. Q. Yue, H. Wu, Z. Zhou, M. Zhang, F. Liu, and X. Zhu, "13.7% Efficiency Small-Molecule Solar Cells Enabled by a Combination of Material and Morphology Optimization," *Advanced Materials* 31 (2019): 1904283.

33. J. Min, X. Jiao, I. Ata, et al., "Time-Dependent Morphology Evolution of Solution-Processed Small Molecule Solar Cells During Solvent Vapor Annealing," *Advanced Energy Materials* 6 (2016): 1502579.

34. M. Li, F. Liu, X. Wan, et al., "Subtle Balance between Length Scale of Phase Separation and Domain Purification in Small-Molecule Bulk-Heterojunction Blends Under Solvent Vapor Treatment," *Advanced Materials* 27 (2015): 6296.

35. W. Zhu, A. P. Spencer, S. Mukherjee, et al., "Crystallography, Morphology, Electronic Structure, and Transport in Non-Fullerene/Non-Indacenodithienothiophene Polymer:Y6 Solar Cells," *Journal of the American Chemical Society* 142 (2020): 14532–14547.

36. K. Gao, W. Deng, L. Xiao, et al., "New Insight of Molecular Interaction, Crystallization and Phase Separation in Higher Performance Small Molecular Solar Cells via Solvent Vapor Annealing," *Nano Energy* 30 (2016): 639–648.

37. Y. Chen, K. Li, J. Zhang, et al., "Over 19% Efficiency Polymer Solar Cells Enabled by Selectively Tuning Bulkheterojunction Morphology via a Dual-Heating Strategy," *Small Methods* 9 (2025): e01159.

38. J. Hao, Y. Feng, Q. Ma, et al., "Real-Time Probing of Morphological Evolution and Recrystallization During Solvent Annealing in Blade-Coated All-Polymer Organic Solar Cells Using In Situ X-Ray Scattering," *Advanced Science* 12 (2025): e01823.

39. C. Cui and Y. Li, "Morphology Optimization of Photoactive Layers in Organic Solar Cells," *Aggregate* 2 (2021): e31.

40. Y. Wang, J. Yu, R. Zhang, et al., "Origins of the Open-Circuit Voltage in Ternary Organic Solar Cells and Design Rules for Minimized Voltage Losses," *Nature Energy* 8 (2023): 978–988.

41. Y. Li, Y. Cai, Y. Xie, et al., "A Facile Strategy for Third-Component Selection in Non-Fullerene Acceptor-Based Ternary Organic Solar Cells," *Energy & Environmental Science* 14 (2021): 5009.

42. L. J. A. Koster, V. D. Mihailetchi, R. Ramaker, and P. W. M. Blom, "Light Intensity Dependence of Open-Circuit Voltage of Polymer:Fullerene Solar Cells," *Applied Physics Letters* 86 (2005): 123509.

43. A. K. K. Kyaw, D. H. Wang, V. Gupta, et al., "Intensity Dependence of Current–Voltage Characteristics and Recombination in High-Efficiency Solution-Processed Small-Molecule Solar Cells," *ACS Nano* 7 (2013): 4569–4577.

44. V. D. Mihailetchi, L. J. A. Koster, J. C. Hummelen, and P. W. M. Blom, "Photocurrent Generation in Polymer-Fullerene Bulk Heterojunctions," *Physical Review Letter* 93 (2004): 216601.

45. W. Zhong, J. Cui, B. Fan, et al., "Enhanced Photovoltaic Performance of Ternary Polymer Solar Cells by Incorporation of a Narrow-Bandgap Nonfullerene Acceptor," *Chemistry of Materials* 29 (2017): 8177–8186.

46. M. Stephen, K. Genevičius, G. Juška, K. Arlauskas, and R. C. Hiorns, "Charge Transport and Its Characterization Using Photo- CELIV in Bulk Heterojunction Solar Cells," *Polymer International* 66 (2017): 13–25.

47. M. E. Ziffer, S. B. Jo, H. Zhong, et al., "Long-Lived, Non-Geminate, Radiative Recombination of Photogenerated Charges in a Polymer/Small-Molecule Acceptor Photovoltaic Blend," *Journal of the American Chemical Society* 140 (2018): 9996–10008.

48. Y. Liu, L. Zuo, X. Shi, A. K. Y. Jen, and D. S. Ginger, "Unexpectedly Slow yet Efficient Picosecond to Nanosecond Photoinduced Hole-Transfer Occurs in a Polymer/Nonfullerene Acceptor Organic Photovoltaic Blend," *ACS Energy Letters* 3 (2018): 2396–2403.

49. C. Huang, D. Kim, W. Yang, et al., "Amphiphilic Polymer Conetworks for Non-Fullerene Organic Solar Cells: Regulated Molecular Stacking Enables Efficient Downconversion," *Advanced Energy Materials* 16 (2025): e04273.

50. G. Xie, J. Wang, J. Lv, et al., "Fully Locked Conjugated Backbones in Simple-Structured Polymer Donors Enabling High-Performance Organic Solar Cells," *Angewandte Chemie International Edition* 137 (2025): e18567.

51. W. Zhang, J. Huang, J. Xu, et al., "Phthalimide Polymer Donor Guests Enable Over 17% Efficient Organic Solar Cells via Parallel-like Ternary and Quaternary Strategies," *Advanced Energy Materials* 10 (2020): 2001436.

52. K. Jiang, J. Lu, R. J. E. Westbrook, et al., "Photoluminescent Delocalized Excitons in Donor Polymers Facilitate Efficient Charge Generation for High-Performance Organic Photovoltaics," *Nature Communications* 16 (2025): 3176.

53. M. Zhang, L. Zhu, T. Hao, et al., "High-Efficiency Organic Photovoltaics Using Eutectic Acceptor Fibrils to Achieve Current Amplification," *Advanced Materials* 33 (2021): 2007177.

54. Y. Wei, X. Zhou, Y. Cai, et al., "High Performance as-Cast Organic Solar Cells Enabled by a Refined Double-Fibril Network Morphology and Improved Dielectric Constant of Active Layer," *Advanced Materials* 36 (2024): 2403294.

55. J. Song, C. Li, H. Ma, et al., "Optimizing Double-Fibril Network Morphology via Solid Additive Strategy Enables Binary All-Polymer Solar Cells With 19.50% Efficiency," *Advanced Materials* 36 (2024): 2406922.

56. B. A. Collins, Z. Li, J. R. Tumbleston, E. Gann, C. R. McNeill, and H. Ade, "Absolute Measurement of Domain Composition and Nanoscale Size Distribution Explains Performance in PTB7:PC 71 BM Solar Cells," *Advanced Energy Materials* 3 (2013): 65–74.

57. D. Kroh, F. Eller, K. Schötz, et al., "Identifying the Signatures of Intermolecular Interactions in Blends of PM6 With Y6 and N4 Using Absorption Spectroscopy," *Advanced Functional Materials* 32 (2022): 2205711.

58. G. Zhang, X. K. Chen, J. Xiao, et al., "Delocalization of Exciton and Electron Wavefunction in Non-Fullerene Acceptor Molecules Enables Efficient Organic Solar Cells," *Nature Communications* 11 (2020): 3943.

59. H. Zhang, C. Tian, Z. Zhang, et al., "Concretized Structural Evolution Supported Assembly-Controlled Film-Forming Kinetics in Slot-Die Coated Organic Photovoltaics," *Nature Communications* 14 (2023): 6312.

60. E. Sebastian, A. M. Philip, A. Benny, and M. Hariharan, "Null Exciton Splitting in Chromophoric Greek Cross(+) Aggregate," *Angewandte Chemie International Edition* 57 (2018): 15696–15701.

61. M. Kasha, "Energy Transfer Mechanisms and the Molecular Exciton Model for Molecular Aggregates," *Radiation Research* 20 (1963): 55.

62. M. Kasha, H. R. Rawls, and M. A. El-Bayoumi, "The Exciton Model in Molecular Spectroscopy," *Pure and Applied Chemistry* 11 (1965): 371–392.

Supporting Information

Additional supporting information can be found online in the Supporting Information section.

Supporting File: agt270305-sup-0001-SuppMat.docx.